Strong Local Coordination Structure Effects on Subnanometer PtO$_x$ Clusters over CeO$_2$ Nanowires Probed by Low-Temperature CO Oxidation

Jun Ke,[†] Wei Zhu,[†] Yingying Jiang,[§] Rui Si,*[,∥] Yan-Jie Wang,[†] Shuai-Chen Li,[†] Chuanhong Jin,[§] Haichao Liu,*[,‡] Wei-Guo Song,[⊥] Chun-Hua Yan,[†] and Ya-Wen Zhang*[,†]

[†]Beijing National Laboratory for Molecular Sciences (BNLMS), State Key Laboratory of Rare Earth Materials Chemistry and Applications, PKU-HKU Joint Laboratory in Rare Earth Materials and Bioinorganic Chemistry, and [‡]Beijing National Laboratory for Molecular Sciences (BNLMS), State Key Laboratory for Structural Chemistry of Stable and Unstable Species, College of Chemistry and Molecular Engineering, Peking University, Beijing 100871, China.

[§]State Key Laboratory of Silicon Materials, Key Laboratory of Advanced Materials and Applications for Batteries of Zhejiang Province, School of Materials Science and Engineering, Zhejiang University, Hangzhou 310027, China.

[∥]Shanghai Synchrotron Radiation Facility, Shanghai Institute of Applied Physics, Chinese Academy of Sciences, Shanghai 201204, China.

[⊥]Beijing National Laboratory for Molecular Sciences (BNLMS), Institute of Chemistry, Chinese Academy of Sciences, Beijing 100190, China.

* Correspondence to: ywzhang@pku.edu.cn, sirui@sinap.ac.cn, hcliu@pku.edu.cn
.
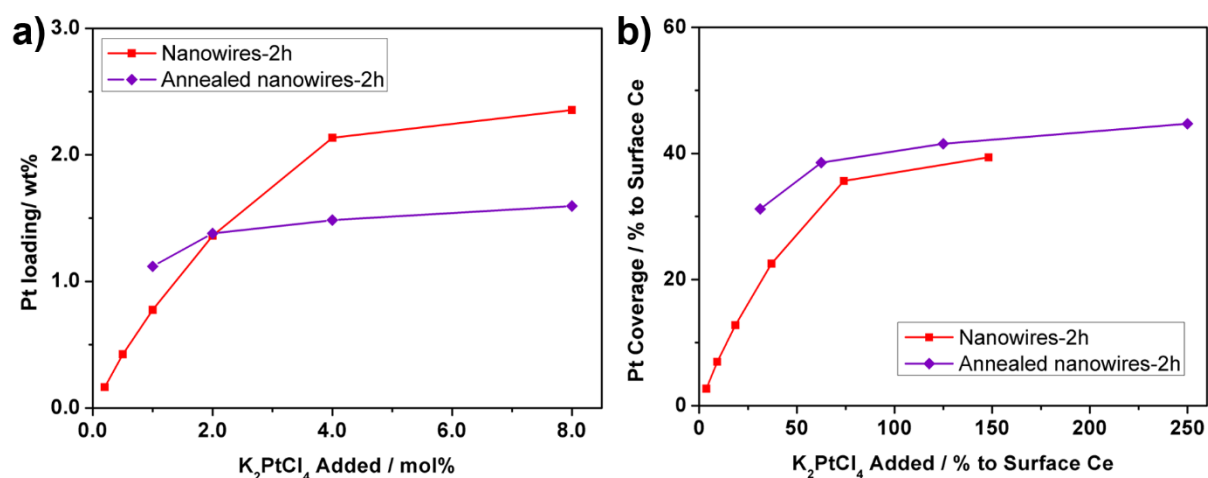
Figure S1. Pt deposition on CeO_2 NWs. (a) Pt loading on CeO_2 NWs with the amount of K_2PtCl_4 added (to total Ce) after the deposition of Pt to the NWs. (b) Pt coverage on CeO_2 NWs with the amount of K_2PtCl_4 added (to surface Ce) after the deposition of Pt to the NWs. Pt coverage was the ratio of total Pt to surface Ce. Pt loading was obtained from ICP-AES analysis. Surface Ce was calculated from BET surface area and the surface density of exposed CeO_2 facets (Ref. 1).
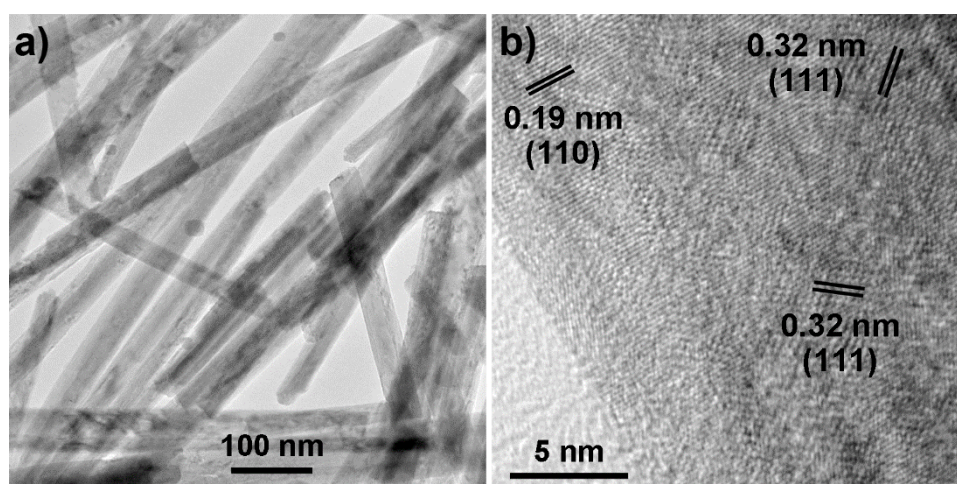
Figure S2. TEM (a) and HRTEM (b) images of the sample of 1.3% PtO_x/CeO_2 NWs-140. (110) facets of the ceria NWs were exposed.
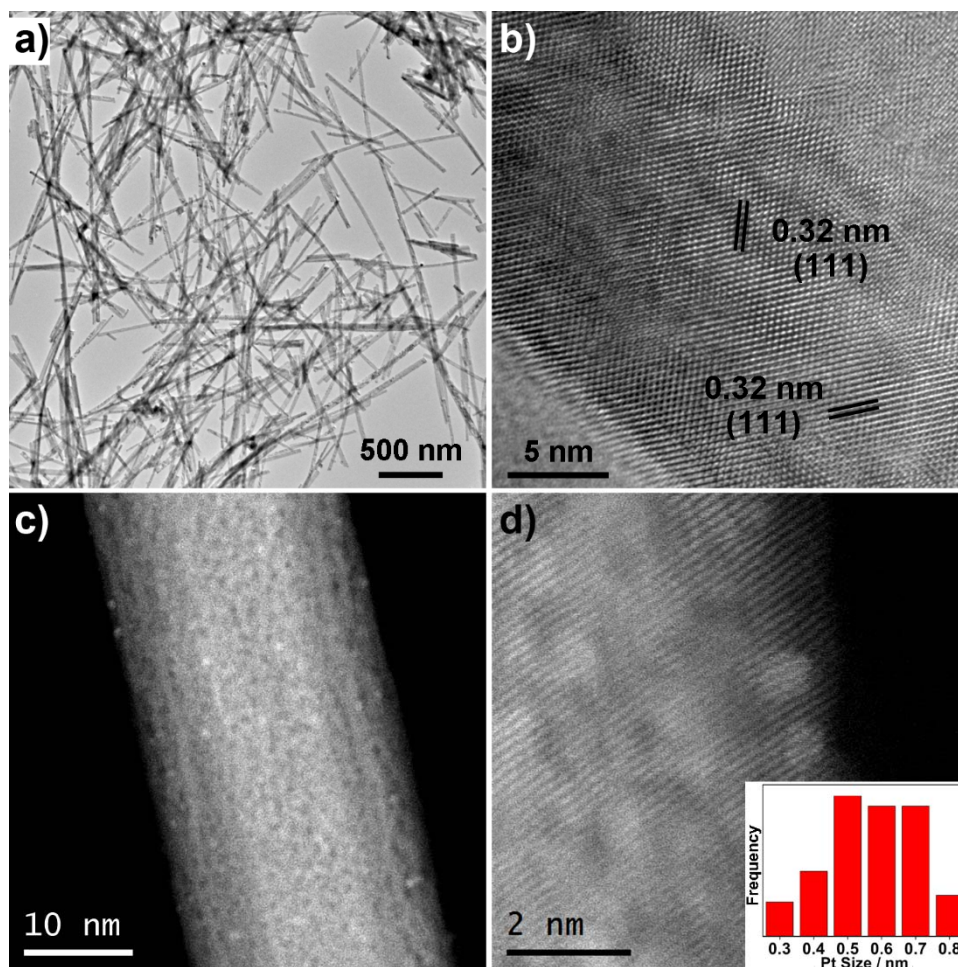
Figure S3. TEM (a), HRTEM (b), and STEM (c, d) images of the sample of 0.42% PtO_x/CeO_2 NWs-350. (110) facets of the ceria NWs were exposed. The insert in panel (d) shows the size distribution of the PtO_x clusters obtained from measuring the size of over 150 clusters.
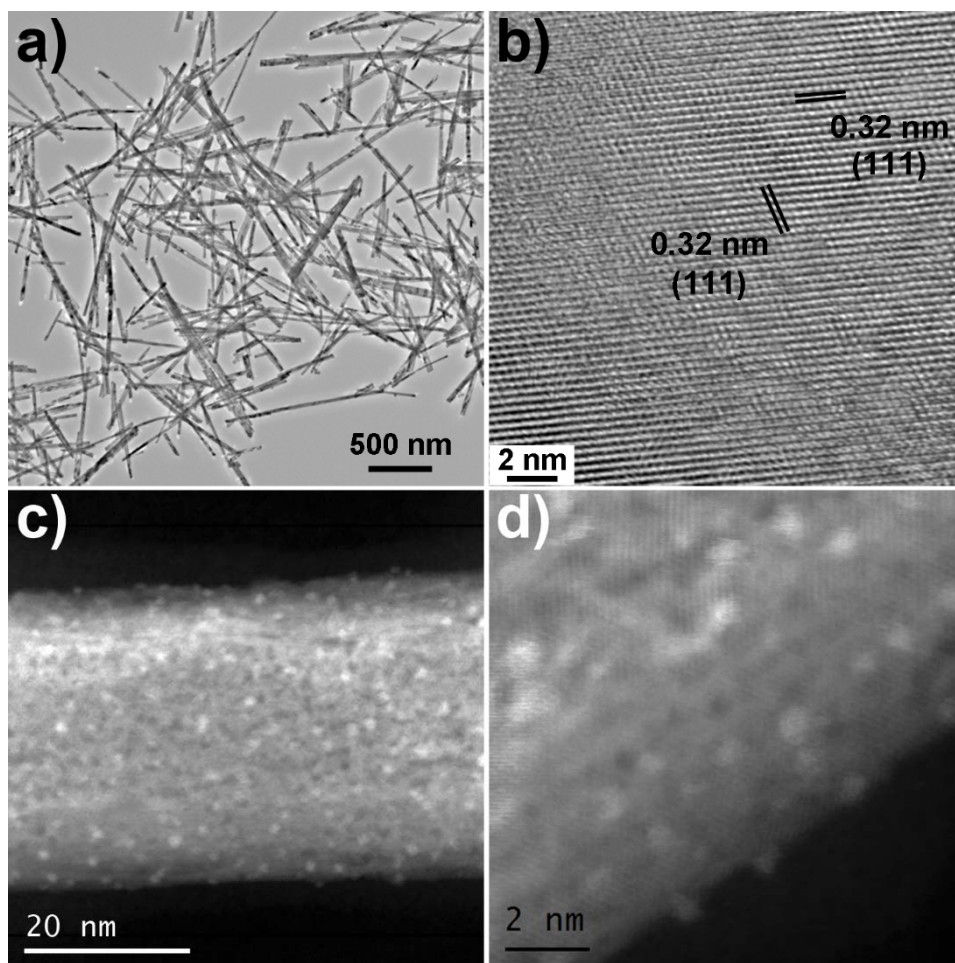
Figure S4. TEM (a), HRTEM (b), and STEM (c, d) images of the sample of 1.3% PtO_x/CeO_2 NWs-350. (110) facets of the ceria NWs were exposed. In the STEM images, the light spots in high contrast represented the PtO_x clusters in which several Pt atoms were close to each other. There were 10−20 of these spots on each 100 nm^2 of the surface of the NWs (39 $m^2 \cdot g^{-1}$ according to BET analysis). Taking the middle value, there would be 6×10^{18} such spots on each gram of the NWs. If there assumed to be at least 4 Pt atoms in each spot, at least 60% of Pt atoms were located in these light spots. It was also possible that the STEM images could miss some PtO_x cluster in smaller scales (*e.g.* Pt_1O_x and Pt_2O_x clusters) because of the similar Z-square numbers for Ce and Pt.

Table S1. Particle size of Pt on CeO_2 NWs.

Sample	Pt size[a] / nm
0.42% PtO_x/CeO_2 NWs-350	0.6±0.1
1.3% PtO_x/CeO_2 NWs-350	0.5±0.1
1.3% PtO_x/CeO_2 NWs-140	Atomically anchored on CeO_2
1.3% Pt/CeO_2 NWs	10−25[b]
0.42% PtO_x/CeO_2 NWs-350 after catalytic tests	0.6±0.1
1.3% PtO_x/CeO_2 NWs-350 after catalytic tests	0.5±0.1

[a] Measured from aberration corrected STEM images.

[b] The 10−25 nm Pt particles with the shapes that similar to the aggregations of small particles with the particle size of 2−4 nm. There were also some aggregations with larger size.
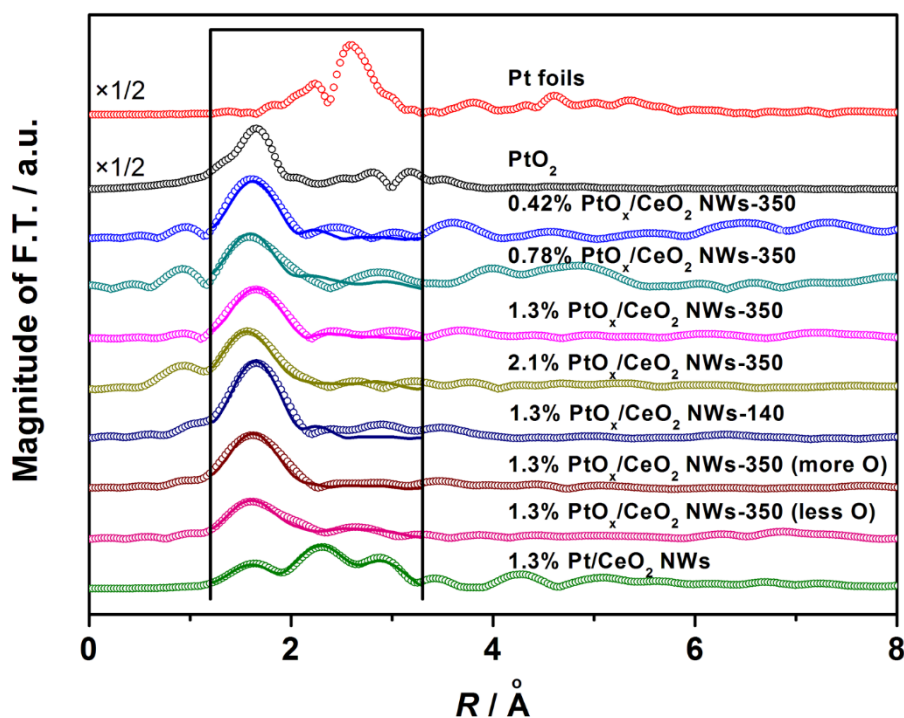
Figure S5. Fourier transforms of EXAFS spectra of Pt L_3 edge and the curve fitting. The dots represent the experimental data while the solid lines represent the fitted data. The window represents the range in *r* space involved in the fitting. Fitting of the Pt−O and the Pt−Pt shell was performed in real space with $\Delta k = 2.7-10$ Å^{-1} and $\Delta R = 1.2-3.3$ Å for Pt (k^2 weighted). S_0^2 was defined as 0.83 for Pt from the fitting of Pt foils.

Table S2. EXAFS parameters for ceria NWs supported Pt nanomaterials.[a]

Sample	Shell	R / Å	CN	σ^2 / Å^2	ΔE_0 / eV
0.42% PtO$_x$/CeO$_2$ NWs-350	Pt−O	2.02±0.02	2.5±0.9		
0.78% PtO$_x$/CeO$_2$ NWs-350	Pt−O	2.00±0.01	2.5±0.6		
1.3% PtO$_x$/CeO$_2$ NWs-350	Pt−O	2.01±0.01	2.6±0.3		
2.1% PtO$_x$/CeO$_2$ NWs-350	Pt−O	2.01±0.01	2.5±0.3		9.3±1.0
1.3% PtO$_x$/CeO$_2$ NWs-140	Pt−O	2.03±0.01	3.8±0.3	0.002±0.001	
1.3% PtO$_x$/CeO$_2$ NWs-350 (less O)	Pt−O	2.03±0.02	2.0±0.3		
1.3% PtO$_x$/CeO$_2$ NWs-350 (more O)	Pt−O	2.01±0.01	3.1±0.3		
1.3% Pt/CeO$_2$ NWs	Pt−O	1.96±0.01	0.7±0.4	0.002±0.002	3.8±0.6
	Pt−Pt	2.75±0.01	7.6±0.8	0.004±0.001	

[a] CN, coordination number; R, interatomic distance between absorber and backscatter atoms; σ^2, Debye–Waller-type factor; ΔE_0, difference between the zero kinetic energy of the sample and that of the model used in the fitting. Athena and Artemis codes were used to extract the data and fit the curve, respectively. Fitting of the Pt−O and the Pt−Pt shell was performed in real space with $\Delta k = 2.7−10$ Å^{-1} and $\Delta R = 1.2−3.3$ Å for Pt (k^2 weighted). S_0^2 was defined as 0.83 for Pt from the fitting of Pt foils. See Figure S5 for the fitting curves.
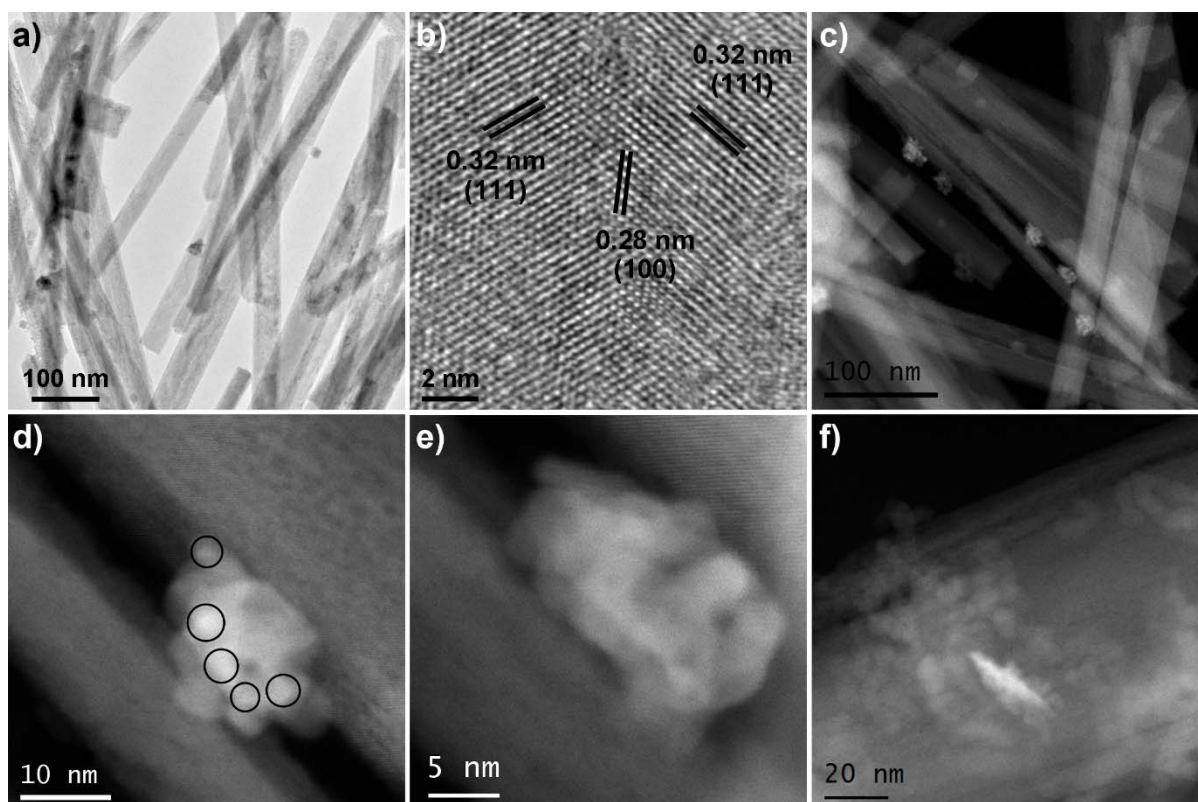
Figure S6. TEM (a), HRTEM (b), and STEM (c−f) images of the sample of 1.3% Pt/CeO$_2$ NWs. (110) facets of the ceria support were exposed. The particle size was about 10−25 nm. According to the difference of the brightness in a representative particle in panel (d, e), the particles seemed to be made up of severely aggregated small parts as small as 2−4 nm (marked with the black circles in panel (d)). There were also some aggregations with larger size (f).
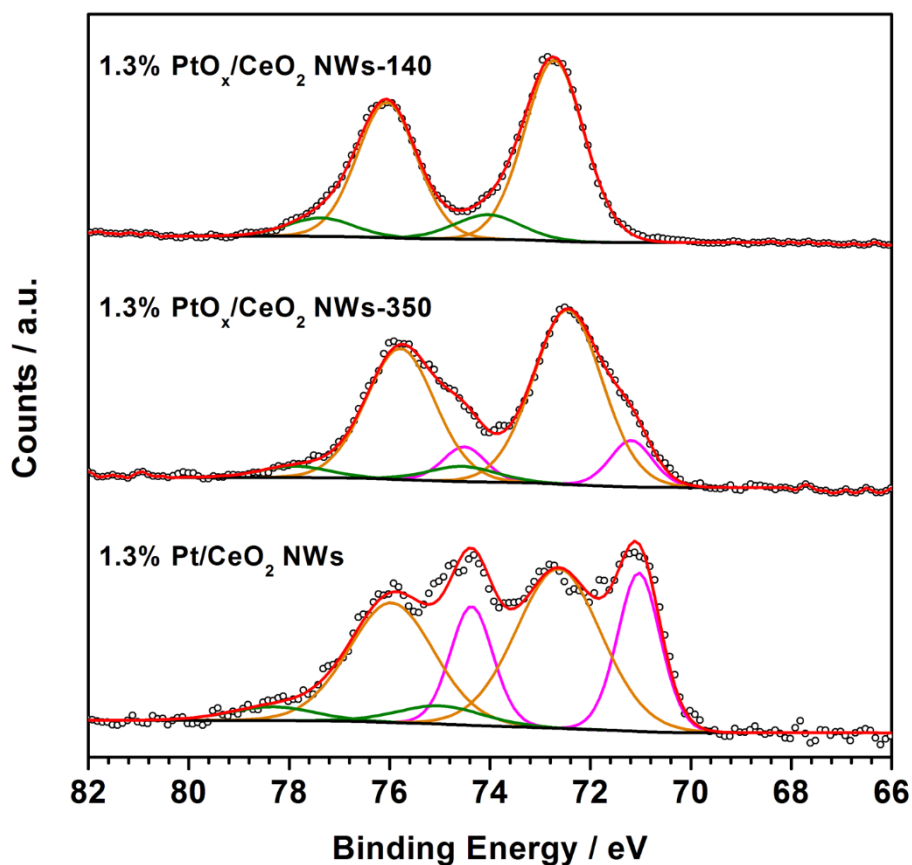
Figure S7. XPS Pt 4f spectra and the fitting of the valence population for the samples of PtO$_x$/CeO$_2$ NWs-140, 1.3% PtO$_x$/CeO$_2$ NWs-350, and 1.3% Pt/CeO$_2$ NWs. The magenta, orange, and green curves represents the Pt in Pt(0), Pt(II), and Pt(IV), respectively. During the curve fitting, for each pair of peaks that represented Pt(0), Pt(II), or Pt(IV), the ratio of 4f$_{5/2}$ peak area to 4f$_{7/2}$ peak area was set to 3:4, and FWHM of the paired peaks was set to be the same, and the difference of the position of the paired peaks was set to 3.33 eV. FWHM was set to be less than 1 eV for the Pt(0) peaks and less than 2 eV for the Pt(II) and Pt(IV) peaks.

Table S3. Valence population of surface Pt on ceria NWs supported Pt nanomaterials according to the fitting of the XPS Pt 4f spectra[a].

Sample	Pt(0) / %	Pt(II) / %	Pt(IV) / %
0.42% PtO$_x$/CeO$_2$ NWs-350	12	81	7
0.78% PtO$_x$/CeO$_2$ NWs-350	12	76	12
1.3% PtO$_x$/CeO$_2$ NWs-350	13	79	8
2.1% PtO$_x$/CeO$_2$ NWs-350	11	79	10
1.3% PtO$_x$/CeO$_2$ NWs-140	0	88	12
1.3% PtO$_x$/CeO$_2$ NWs-350 (less O)	11	82	7
1.3% PtO$_x$/CeO$_2$ NWs-350 (more O)	8	77	5
1.3% Pt/CeO$_2$ NWs	32	61	7

[a] During the fitting of each spectra, for each pair of peaks that represented Pt(0), Pt(II), or Pt(IV), the ratio of 4f$_{5/2}$ peak area to 4f$_{7/2}$ peak area was set to 3:4, and the full width at half maximum (FWHM) of the paired peaks was set to be the same, and the difference of the position of the paired peaks was set to 3.33 eV. FWHM was set to be less than 1 eV for the Pt(0) peaks and less than 2 eV for the Pt(II) and Pt(IV) peaks. The data in this table gives qualitative results that Pt was mainly in Pt(II) in our PtO$_x$/CeO$_2$ NWs samples rather than quantitative data of the ratio of each Pt species because the Pt(0) and Pt(IV) peaks were in the tails of Pt(II) peaks.

Table S4. Valence population of surface Ce on ceria NWs supported Pt nanomaterials according to the fitting of the XPS Ce 3d spectra.[a]

Sample	Ce^{3+} / %	Ce^{4+} / %
CeO$_2$ NWs	undetected	100
0.42% PtO$_x$/CeO$_2$ NWs-350	undetected	100
0.78% PtO$_x$/CeO$_2$ NWs-350	undetected	100
1.3% PtO$_x$/CeO$_2$ NWs-350	undetected	100
2.1% PtO$_x$/CeO$_2$ NWs-350	undetected	100
1.3% PtO$_x$/CeO$_2$ NWs-140	undetected	100
1.3% PtO$_x$/CeO$_2$ NWs-350 (less O)	undetected	100
1.3% PtO$_x$/CeO$_2$ NWs-350 (more O)	undetected	100
1.3% Pt/CeO$_2$ NWs	undetected	100

[a] Ce 3d spectra of the samples were fitted as the linear combination of Ce(III) and Ce(IV) 3d spectra with the reported method (Ref. 2).
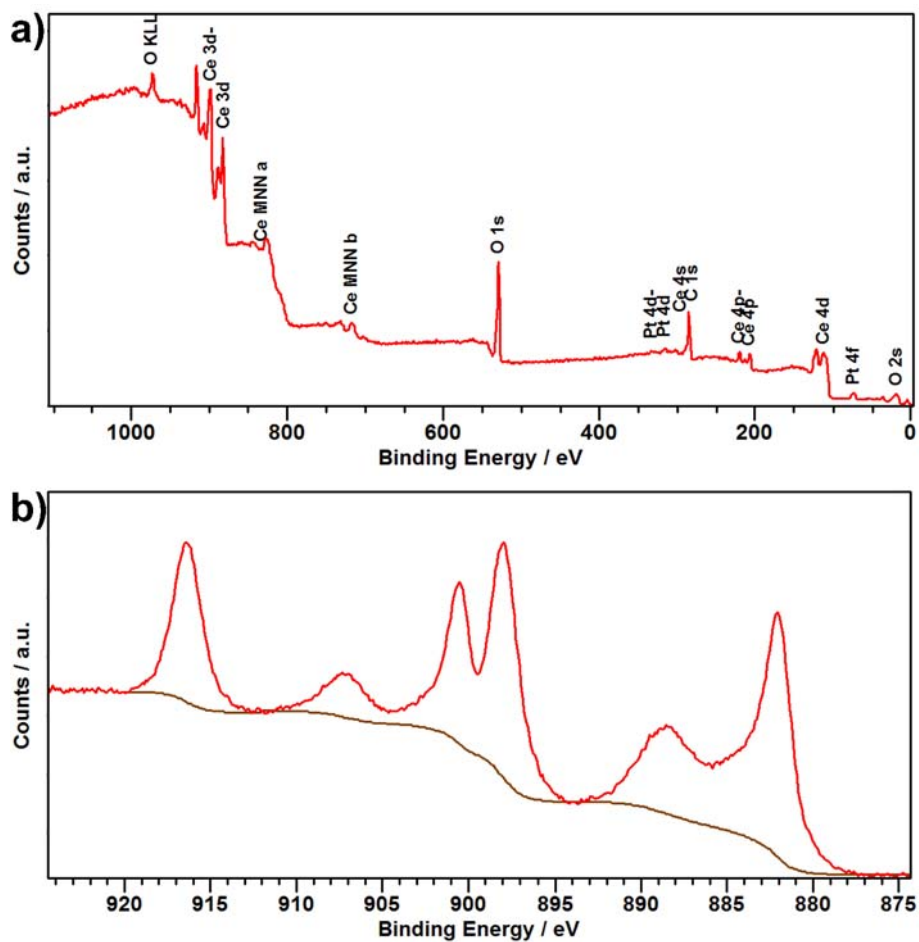
Figure S8. XPS spectra of representative sample of 1.3% PtO$_x$/CeO$_2$ NWs-350. (a) Full spectra. (b) Ce 3d spectra. Ce 3d spectra were fitted with the spectra of pure CeO$_2$ and Ce$_2$O$_3$ to estimate the ratio of Ce^{3+}/Ce^{4+} with the reported method (Ref. 2). Ce^{3+} was undetected from the fitting.

Table S5. Catalytic activity on CO oxidation over ceria NWs supported Pt catalysts.

Sample	Pt dispersion / %	Exposed Pt[b] / wt%	Specific activity at 50 °C / $mmol \cdot g_{cat}^{-1} \cdot h^{-1}$	TOF at 50 °C[c] / s^{-1}
0.42% PtO$_x$/CeO$_2$ NWs-350	100	0.42	1.0	1.3×10^{-2}
0.78% PtO$_x$/CeO$_2$ NWs-350	83	0.64	1.3	1.1×10^{-2}
1.3% PtO$_x$/CeO$_2$ NWs-350	68	0.88	1.8	1.1×10^{-2}
2.1% PtO$_x$/CeO$_2$ NWs-350	52	1.1	2.4	1.2×10^{-2}
1.3% PtO$_x$/CeO$_2$ NWs-140	100[a]	1.3[a]	$<10^{-2}$	$<10^{-4}$
1.3% PtO$_x$/CeO$_2$ NWs-350 (less O)	68	0.88	3.2	2.0×10^{-2}
1.3% PtO$_x$/CeO$_2$ NWs-350 (more O)	72	0.94	0.95	5.5×10^{-3}
1.3% Pt/CeO$_2$ NWs	10	0.13	0.041	1.7×10^{-3}

[a] Estimated according to the aberration corrected STEM images because H$_2$ treatment at high temperature would make the Pt grow larger.

[b] Obtained from H$_2$ chemisorption at 20 °C by assuming 1:1 H:Pt adsorption (Ref. 3). The samples were reduced in hydrogen and evacuated at 300 °C before chemisorption measurements. H$_2$ and CO chemisorption gave consistent results for our Pt/CeO$_2$ samples.

[c] TOF was normalized to per exposed surface Pt atom. Exposed surface Pt atom was obtained by chemisorption described in the above footnote. For the sample of 1.3% PtO$_x$/CeO$_2$ NWs-140, every atom was assumed to be exposed.

Table S6. Valence population of surface Ce and Pt on ceria NWs supported Pt nanomaterials after catalytic test.[a]

Sample	Ce(III) / %	Ce(IV) / %	Pt(0) / %	Pt(II) / %	Pt(IV) / %
0.42% PtO$_x$/CeO$_2$ NWs-350	undetected	100	13	80	7
1.3% PtO$_x$/CeO$_2$ NWs-350	undetected	100	15	80	5
1.3% PtO$_x$/CeO$_2$ NWs-140	undetected	100	0	95	5
1.3% PtO$_x$/CeO$_2$ NWs-350 (less O)	undetected	100	11	81	8
1.3% PtO$_x$/CeO$_2$ NWs-350 (more O)	undetected	100	8	85	7
1.3% Pt/CeO$_2$ NWs	undetected	100	31	62	7

[a] During the fitting of each Pt spectra, for each pair of peaks that represented Pt(0), Pt(II), or Pt(IV), the ratio of 4f$_{5/2}$ peak area to 4f$_{7/2}$ peak area was set to 3:4, and the full width at half maximum (FWHM) of the paired peaks was set to be the same, and the difference of the position of the paired peaks was set to 3.33 eV. FWHM was set to be less than 1 eV for the Pt(0) peaks and less than 2 eV for the Pt(II) and Pt(IV) peaks. The valance of Pt did not change much after catalytic tests. Pt was still mainly in Pt(II) in our PtO$_x$/CeO$_2$ NWs samples. The data in this table gives qualitative results rather than quantitative data of the ratio of each Pt species because the Pt(0) and Pt(IV) peaks were in the tails of Pt(II) peaks.
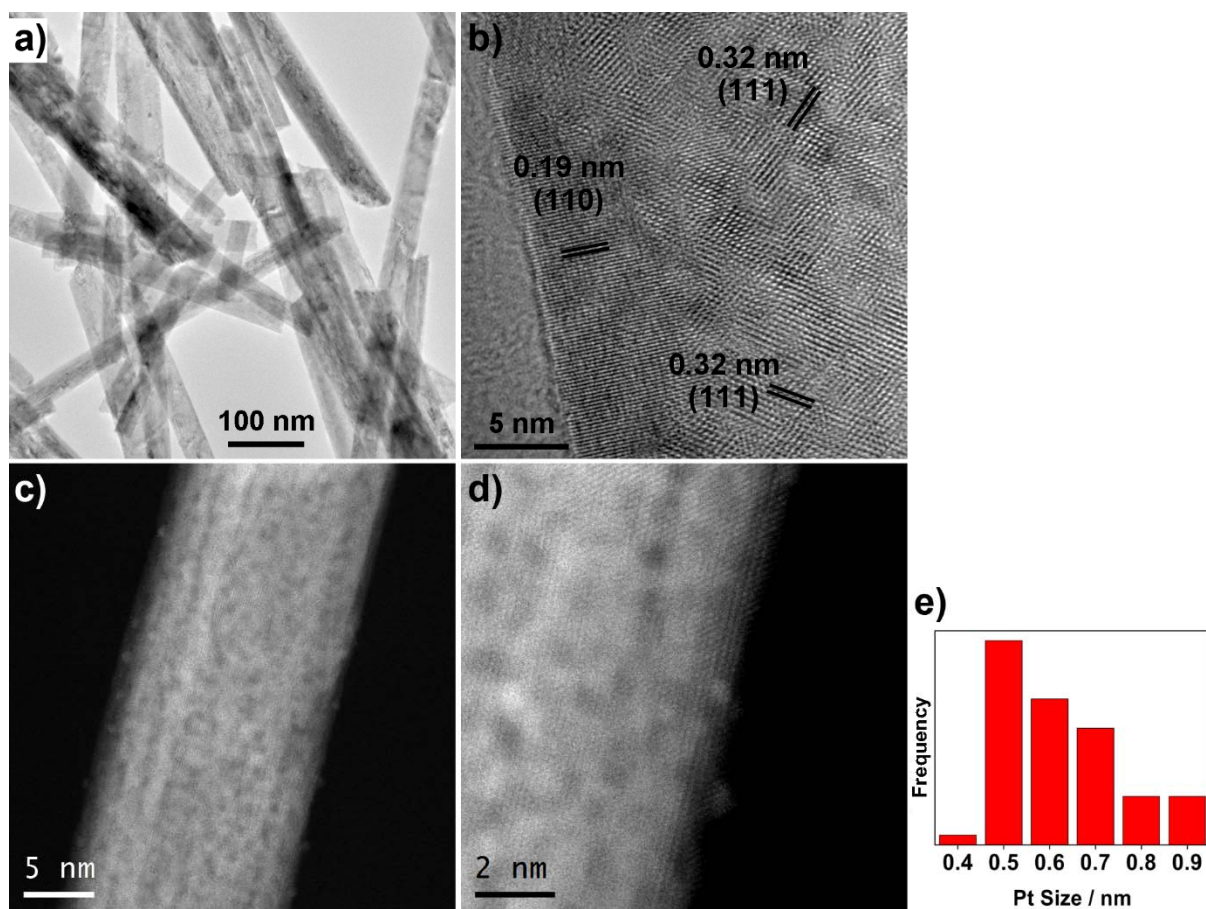
Figure S9. TEM (a), HRTEM (b), and aberration corrected STEM (c, d) images of the sample of 0.42% PtO_x/CeO_2 NWs-350 after catalytic tests. (e) Size distribution of the PtO_x clusters in the sample of 0.42% PtO_x/CeO_2 NWs-350 after catalytic tests. The size distribution was obtained from measuring the size of over 150 clusters. The size and surface morphology for this sample did not change much after catalysis.
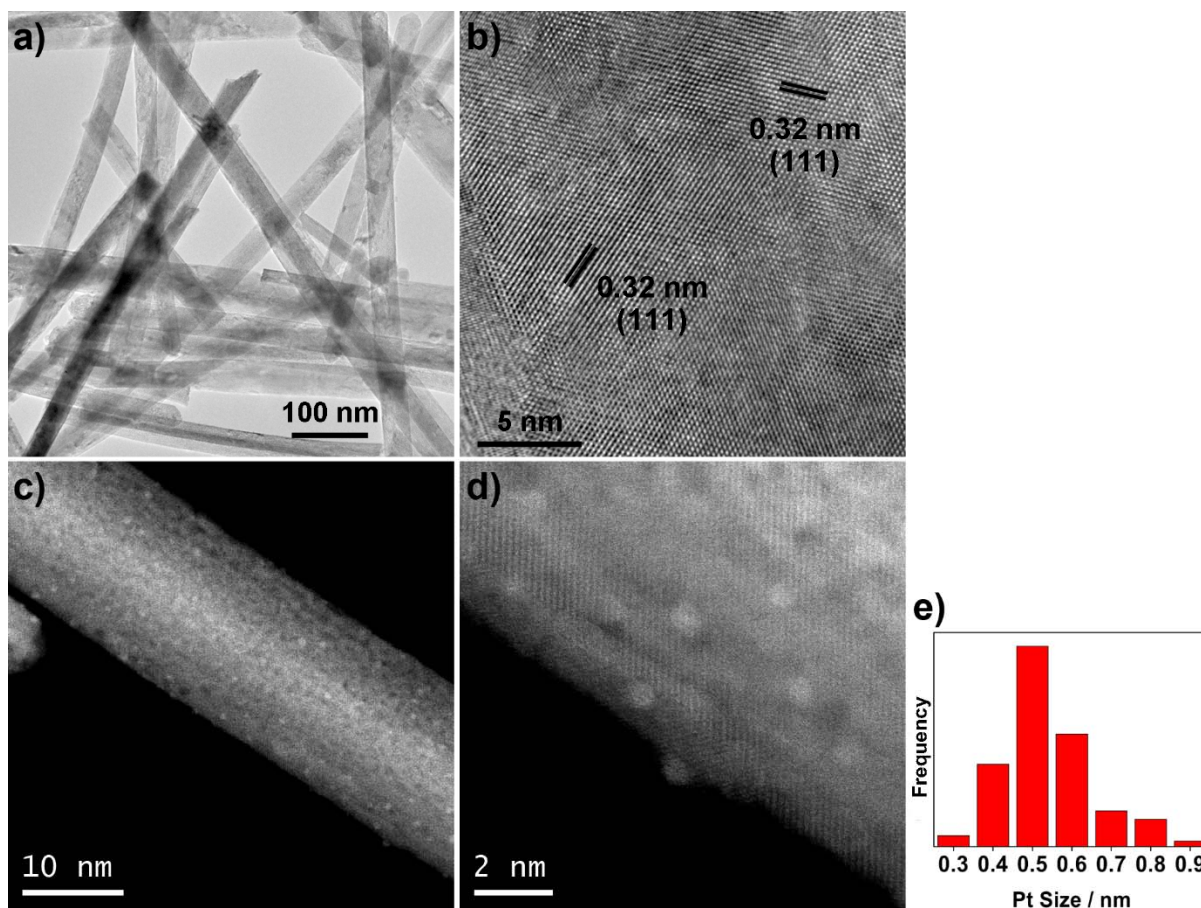
Figure S10. TEM (a), HRTEM (b), and aberration corrected STEM (c, d) images of the sample of 1.3% PtO$_x$/CeO$_2$ NWs-350 after catalytic tests. (e) Size distribution of the PtO$_x$ clusters in the sample of 1.3% PtO$_x$/CeO$_2$ NWs-350 after catalytic tests. The size distribution was obtained from measuring the size of over 150 clusters. The size and surface morphology for this sample did not change much after catalysis.

Table S7. Apparent activation energy of catalytic CO oxidation reactions over ceria NWs supported Pt catalysts.

Sample	Activation energy / $kJ\cdot mol^{-1}$
0.42% PtO_x/CeO_2 NWs-350	65±2
1.3% PtO_x/CeO_2 NWs-350	70±4
1.3% PtO_x/CeO_2 NWs-350 (less O)	65±4
1.3% PtO_x/CeO_2 NWs-350 (more O)	66±2
1.3% Pt/CeO_2 NWs	70±2
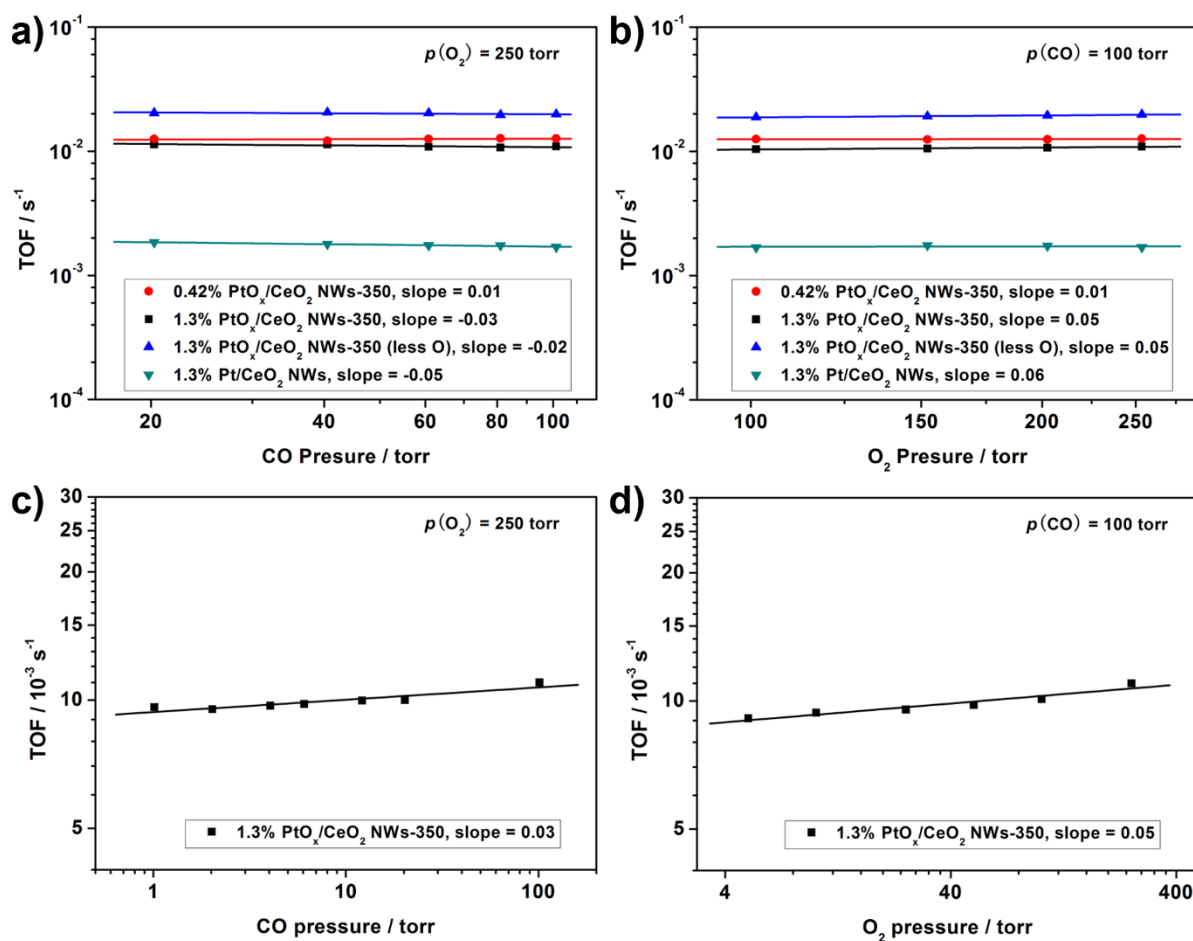
Figure S11. CO oxidation activity over PtO_x/CeO_2 NWs with varied partial pressure of the reactants at 50 °C. (a) Reliance on CO pressure. (b) Reliance on O_2 pressure. (c) Reliance on CO pressure in an enlarged scale (CO-lean conditions). (d) Reliance on O_2 pressure in an enlarged scale (including CO-rich conditions). The change of gas mixtures from CO-lean conditions to CO-rich conditions did not result in a significant change in the effective active site numbers or the activity. Ref. 4 gives one possible kinetic expression that is not in conflict with our experiment results, further work is required before the reaction pathways could be determined.
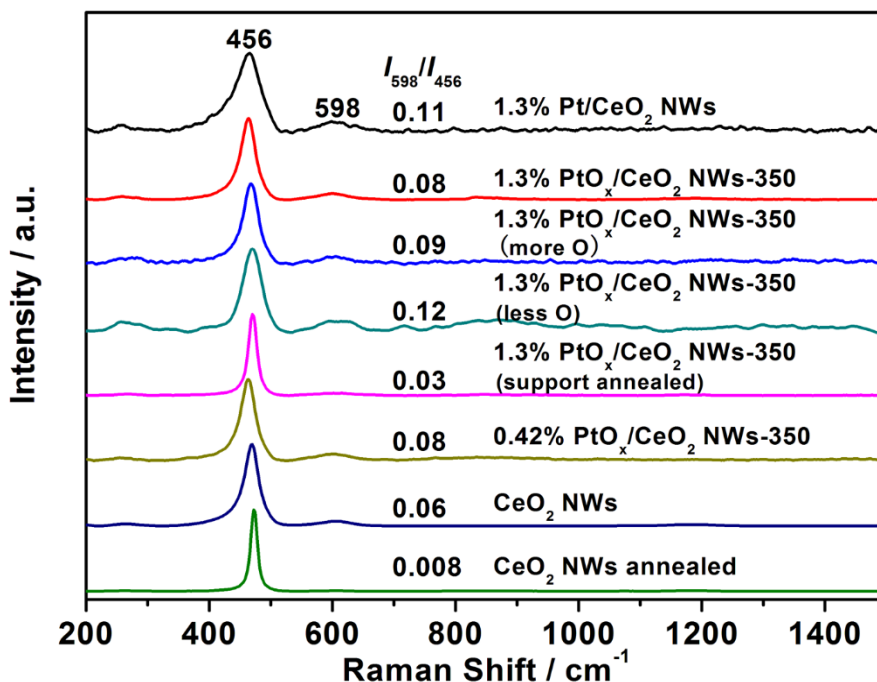
Figure S12. Raman spectra with 488 nm laser excitation for ceria NWs with sub-nano PtO_x clusters. The defects of the ceria support were estimated from the intensity ratio of D mode at 598 cm^{-1} to F_{2g} mode at 498 cm^{-1} ($I(D)/I(F_{2g})$) (Ref. 5). From the consideration that Ce^{3+} was undetected from XPS analysis, the oxygen defects were mainly attributed to the interstitial defects (Ref. 5). The peaks assigned to Pt−O−Ce (550 cm^{-1}) and Pt−O (665 cm^{-1}) were not clearly detected (Ref. 6). As a comparison, the ceria supports were annealed at 600 °C before Pt deposition to obtain a control sample that denoted as 1.3% PtO_x/CeO_2 NWs-350 (support annealed). The $I(D)/I(F_{2g})$ value of the control samples decreased to 0.008 compared to the value of 0.03 for the unannealed sample. But the TOF values of the two samples were very similar (about 1.1×10^{-2} s^{-1} at 50 °C), indicating that the oxygen defects on the supports were not the key factor in determining the active sites for our samples.

Hydroxyls and adsorbed water could be adsorbed onto the surfaces of CeO_2 NWs. CeO_2 was expected to be more suitable for these species to bond rather than Pt atoms. These species could not be the major reason to cause the difference of the activity among our samples. When 2 kPa of water vapor was introduced into the reactants during the CO oxidation, their catalytic activity did not show obvious change.

According to XPS analysis, the ratio of Cl to Ce was similar on pure CeO_2 NWs and all the samples of PtO_x/CeO_2 NWs. The Pt−Cl shell (around 2.2−2.3 Å) was not observed in R space of the EXAFS spectra (Figure S5) and unable to fit. It indicated that the Pt−Cl structure was at least not the major component in the fresh sample, since XAFS is a technique for bulk analysis and averages all the structure contributions. Therefore, Cl was not the major reason to cause the difference of the activity among our samples.
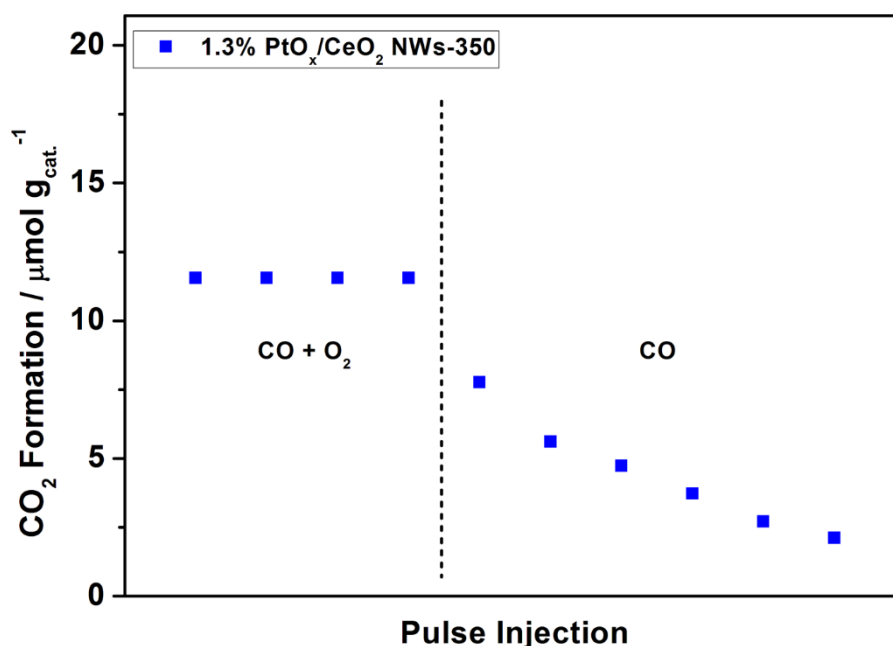
Figure S13. Catalytic performance of the sample of PtO_x/CeO_2 NWs-350 with the pulse injection of reactants. The catalysts were first injected with the pulse of 13.3% CO/33.3% O_2/He at 50 °C. The outlet gas was analysed by GC with a TCD detector. CO conversion was controlled below 15% for each injection. Between each pulse injection, the sample was flowed with He for 15 min to remove the weakly adsorbed moleculars. After the catalyst got stablized, the feeding gas was switched to the pulse of 13.3% CO/He.

According to the apparent kinetic reaction order, in the mixture of CO and O_2, $r = k\ p_{CO}^0\ p_{O_2}^0$. When the gas of pulse became CO, the rate should become $r = k\ p_{CO}^0\ [O_L]$ according to the MVK mechanism. The initial rate should be close to that under CO oxidation conditions. CO conversion in the first pulse of CO remained 70% to that in the mixture of CO and O_2. This result agreed with the features of MVK mechanism.

CO_2 formed in the initial five times of CO pulse was 26 $\mu mol \cdot g_{cat}^{-1}$ (quantified with GC analysis). O_L consumption was 0.4:1 of O_L:Pt.
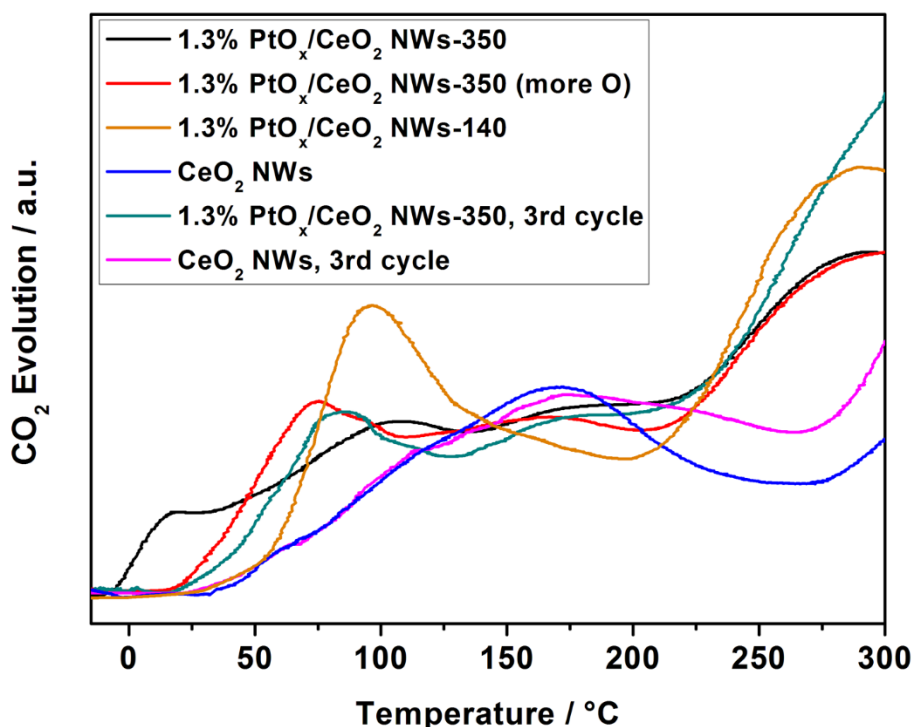
Figure S14. CO-TPR profiles for the samples of 1.3% PtO_x/CeO_2 NWs. Conditions of CO-TPR: The samples (50 mg) were heated at the rate of 5 °C·min^{-1} in the flowing 5% CO/He (20 mL·min^{-1}). CO_2 evolution was obtained from MS signals. Pretreatment for the black, red, and blue curves (represent the first cycle of CO-TPR): The samples were pretreated in He flow at 50 °C for 1 h. Pretreatment for the cyan and magenta curves (represent the third cycle of CO-TPR): The samples were heated to 300 °C (5 °C·min^{-1}) in the flowing 5% CO/He (20 mL·min^{-1}), and then kept in flowing 5% O_2/He for 1 h before cooling down. The above treatment was done again. Then, the samples were treated in He flow at 50 °C for 1 h before the third cycle of CO-TPR analysis.

The difference of CO_2 signal of the PtO_x/CeO_2 NWs samples from that of CeO_2 NWs below 130 °C represented the consumption of oxygen species very close to Pt sites. By comparing the area of this part of CO_2 formation to the total area of CO_2 formation up to over 1000 °C, the active oxygen species were found to be 2.8−3.4:1 and 1.6:1 of O:Pt from the first cycle and the third cycle of CO-TPR for the sample of 1.3% PtO_x/CeO_2 NWs-350, respectively.

The light-off temperature of the first reduction peak for the sample of 1.3% PtO_x/CeO_2 NWs-140 was higher than those for the samples of 1.3% PtO_x/CeO_2 NWs-350, and was similar to that for the support CeO_2 NWs. The low reducibility of the PtO_x clusters on the sample of 1.3% PtO_x/CeO_2 NWs-140 agreed with its low reducibility in the H_2-TPR experiments.
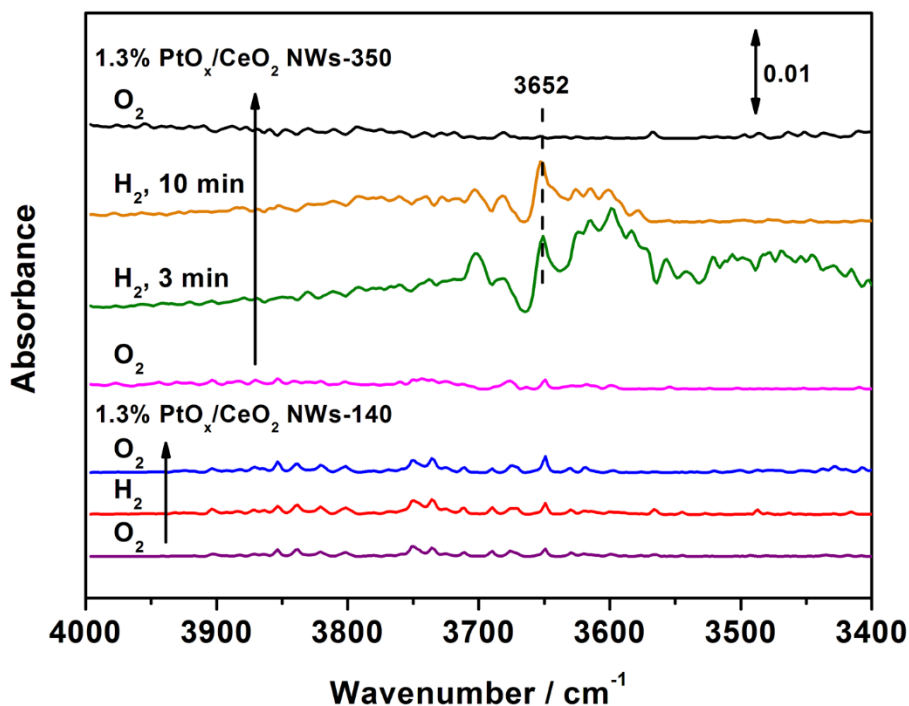
Figure S15. *In-situ* IR spectra of the PtO$_x$/CeO$_2$ NWs samples to show the variation of adsorbed OH species under the consecutive redox treatment at 50 °C. The IR spectra were collected in the diffusion reflection mode. For each sample, the background of the sample was collected in flowing N$_2$ (40 mL·min^{-1}) at 50 °C. Then, the samples were consecutively exposed to flowing (40 mL·min^{-1}) 5% H$_2$/N$_2$, 5% O$_2$/He, and 5% H$_2$/N$_2$, and stabilized in each gas mixture. For the sample of 1.3% PtO$_x$/CeO$_2$ NWs-350, the peak at 3652 cm^{-1} was assigned to the increase of OH species according to Ref. 6. The spillover of hydrogen from the reduced PtO$_x$ sites to ceria caused the surface reduction of CeO$_2$ NWs and the increase of these OH species. When the gas was switched back to O$_2$, the absorbance peak of OH species dispeared, indicating that the surface bonding mode of OH species return to the initial state. For the sample of 1.3% PtO$_x$/CeO$_2$ NWs-140, there was no obvious peak of OH species under either O$_2$ treatment or H$_2$ reduction. The surface bonding mode of OH species did not show obvious change compared to that in N$_2$ when the background of the spectra was collected. This observation agreed to the H$_2$-TPR analysis that showed no obvious H$_2$ consumption peak at or below 50 °C for this sample.
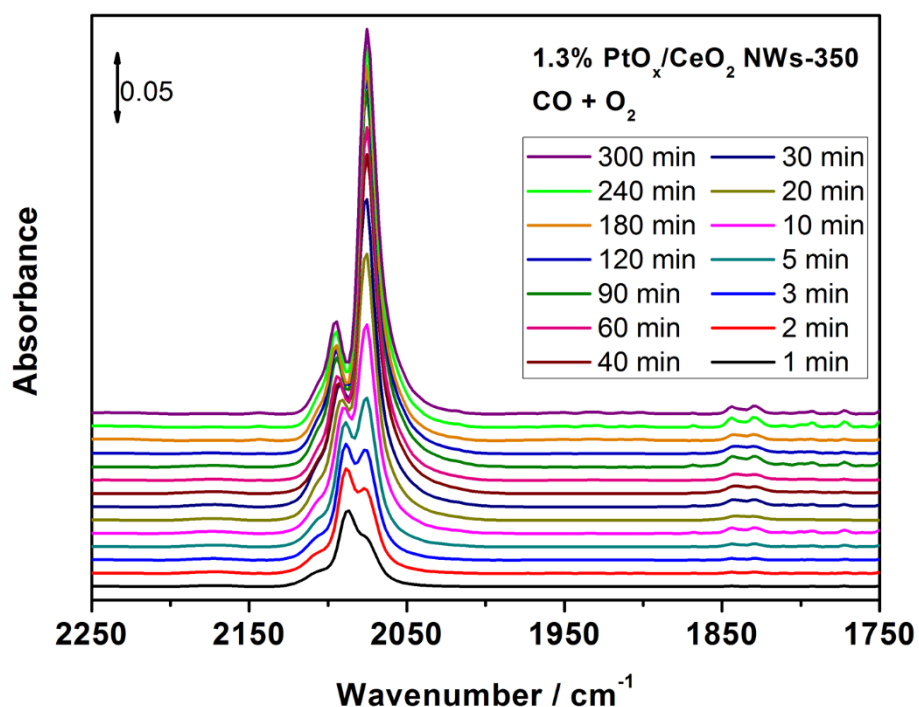
Figure S16. *In-situ* IR spectra of the sample of 1.3% PtO$_x$/CeO$_2$ NWs-350 under CO oxidation conditions (2% CO/5% O$_2$/He) at 50 °C. The peak at 2075 cm^{-1} (Pt^0) increased obviously in the first 30 min. The peak at 2089 cm^{-1} (Pt$^{\delta+}$) shifted to 2096 cm^{-1} in the 5 h of reaction without much change in absorbance of the peak after the initial 1−2 min. There was a shoulder peak around 2103 cm^{-1} (Pt^{2+}).

Table S8. Assignments of surface species in IR spectra.

Species	Wavenumber / cm^{-1}	
	Values in Literatures[a]	Values in this work
gaseous CO	2144-2176	2172
linearly bonded CO on Pt^{2+}	2108-2120	2102-2120
linearly bonded CO on Pt$^{\delta+}$	2075-2092	2086-2092
linearly bonded CO on Pt^0	2044-2086	2066-2085
bridge-bonded CO	1825	1833

[a] Values reported in Refs. 7−13.
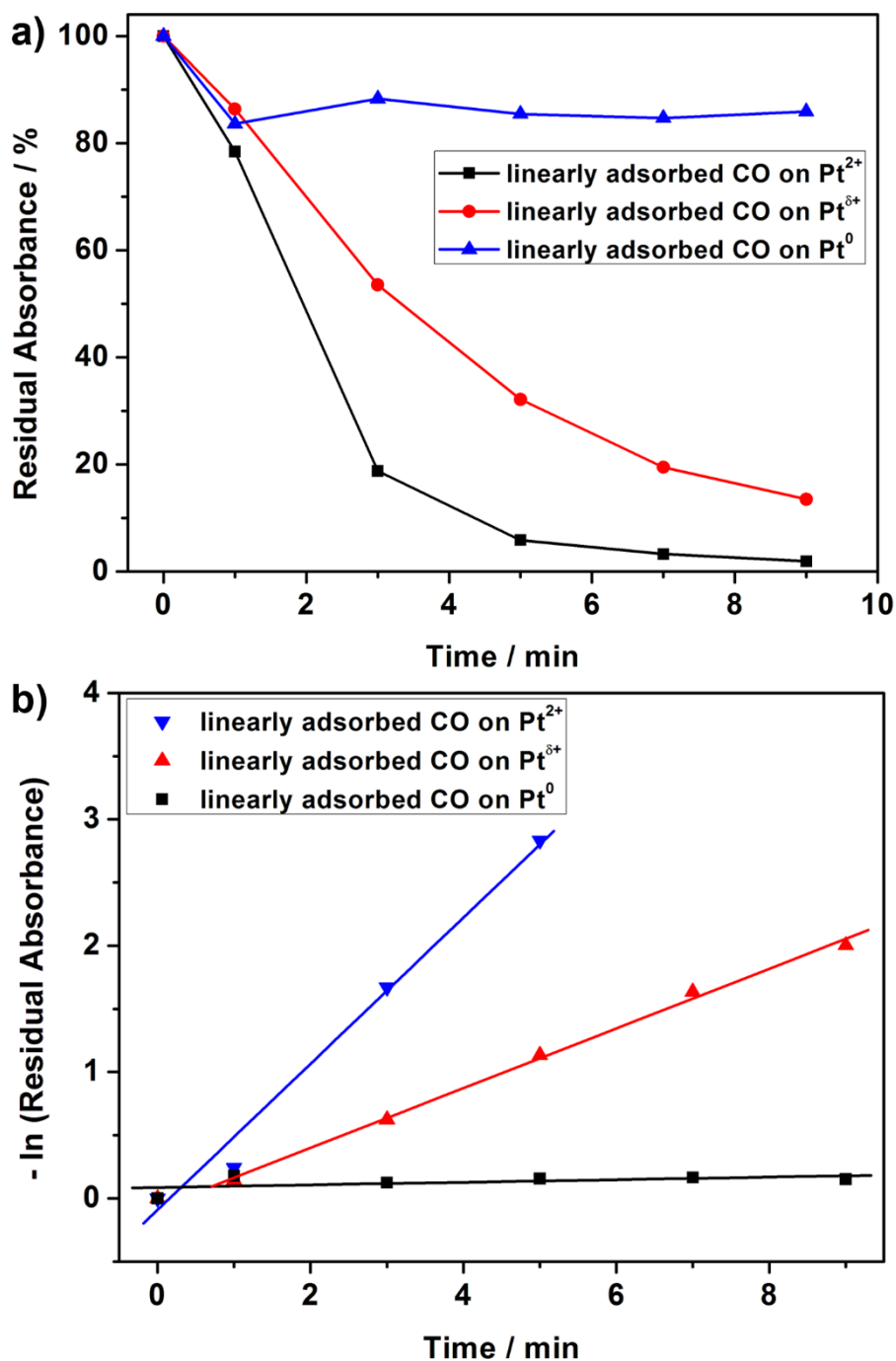
Figure S17. (a) The absorbance variation of linearly adsorbed CO on Pt^{2+}, $Pt^{\delta+}$, and Pt^0 over the sample of 1.3% PtO_x/CeO_2 NWs-350 during the adsorbed CO intermediates reacted with O_2 at 50 C. Before the gas was switched to O_2, the sample was stabilized under CO oxidation conditions (2% CO/5% O_2/He, 50 °C) for 40 min. Thus, the variation of the absorbance represents the reaction between the adsorbed CO intermediates and oxygen species. The absorbance variation was obtained from fitting the curves in Figure 5a with Gaussian peaks. (b) The linear fitting of the absorbance as the 1st order reaction. According to the apparent kinetic reaction order, $r = k\ p_{CO}^0\ p_{O_2}^0$ in the mixture of CO and O_2. When CO was removed

from the feeding gas, the rate should become $r = k \text{ [CO*]} \, p_{O_2}^0$ according to the MVK mechanism. The variation of [CO*] should vary as the 1st order reaction: $\ln(\text{[CO*]}) \propto k\,t$. According to the linear fitting, the rate constant k was 0.010 s^{-1} and 0.0040 s^{-1} for linearly adsorbed CO on Pt^0 and $Pt^{\delta+}$, respectively, with the uncertainty of $\pm 15\%$. The rate constant k was 0.0003 s^{-1} for linearly adsorbed CO on Pt^{2+} with the uncertainty of $\pm 100\%$. There were some possibilities that could explain the sequence of the three apparent rate constants. One possible reason was that the adsorbed CO intermediates on Pt^0 could react faster with oxygen species than those on oxidized Pt sites. Another possible reason was that there was a bigger proportion of inactive CO intermediates on oxidized Pt sites so the apparent rate constant of CO on oxidized Pt sites became small. One more possible reason was that the adsorb CO on Pt^0 moved to oxidized Pt sites first, and then reacted with oxygen species so the apparent rate constant of CO on oxidized Pt sites became smaller than the real value.
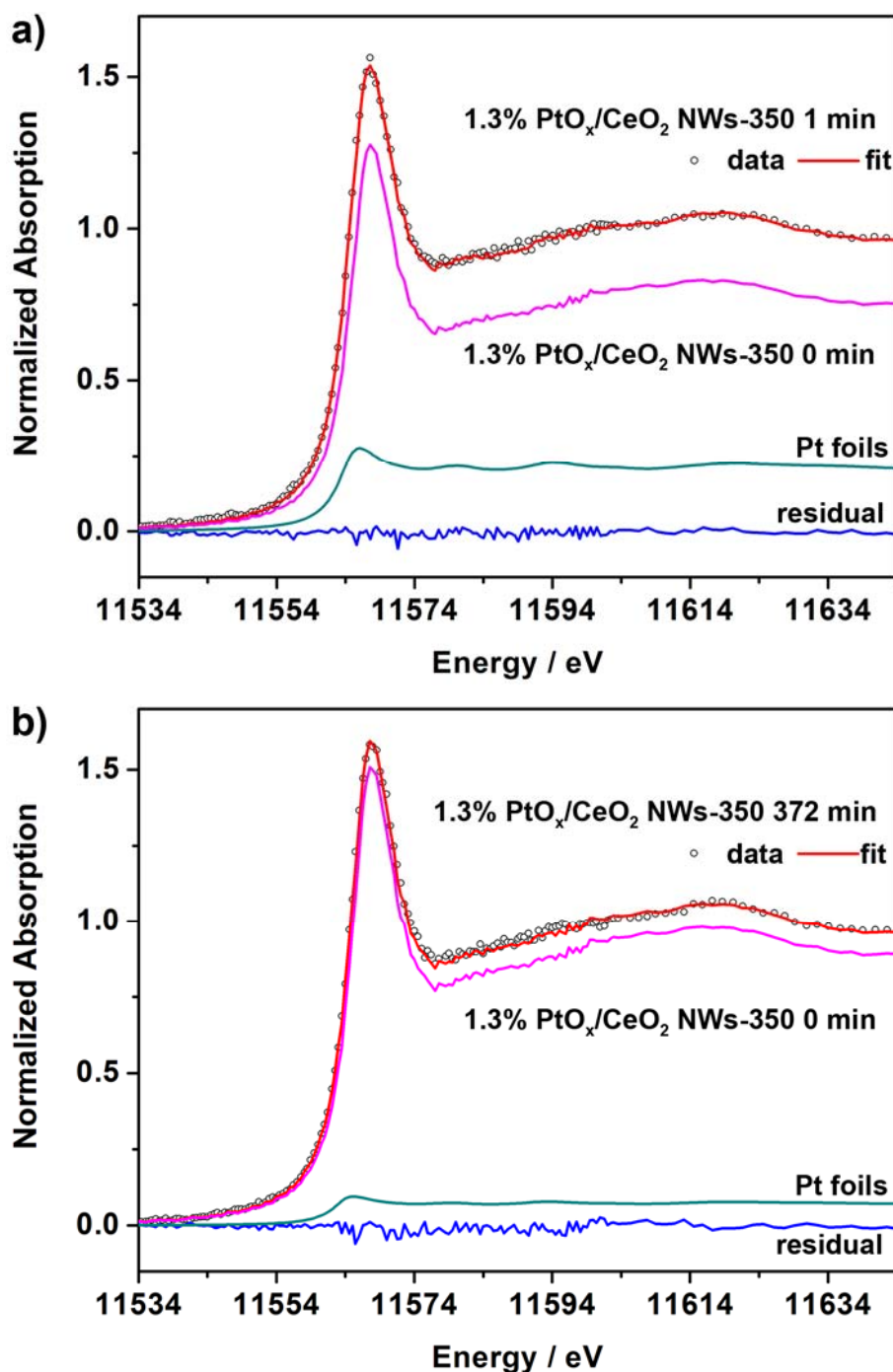
Figure S18. Linear combination fitting of the *in-situ* XANES spectra of the sample of 1.3% PtO$_x$/CeO$_2$ NWs-350 under CO oxidation conditions (2% CO/5% O$_2$/He, 75 °C). The XANES spectra were fitted as the linear combination of the Pt foil spectra and the spectra of the sample of 1.3% PtO$_x$/CeO$_2$ NWs-350 at 0 min. (a) Linear combination fitting of the *in-situ* XANES spectra of the sample of 1.3% PtO$_x$/CeO$_2$ NWs-350 at 1 min. (b) Linear combination fitting of the *in-situ* XANES spectra of the sample of 1.3% PtO$_x$/CeO$_2$ NWs-350 at 372 min. The time of the spectra represents when the collection of the spectra started during the *in-situ* CO oxidation.
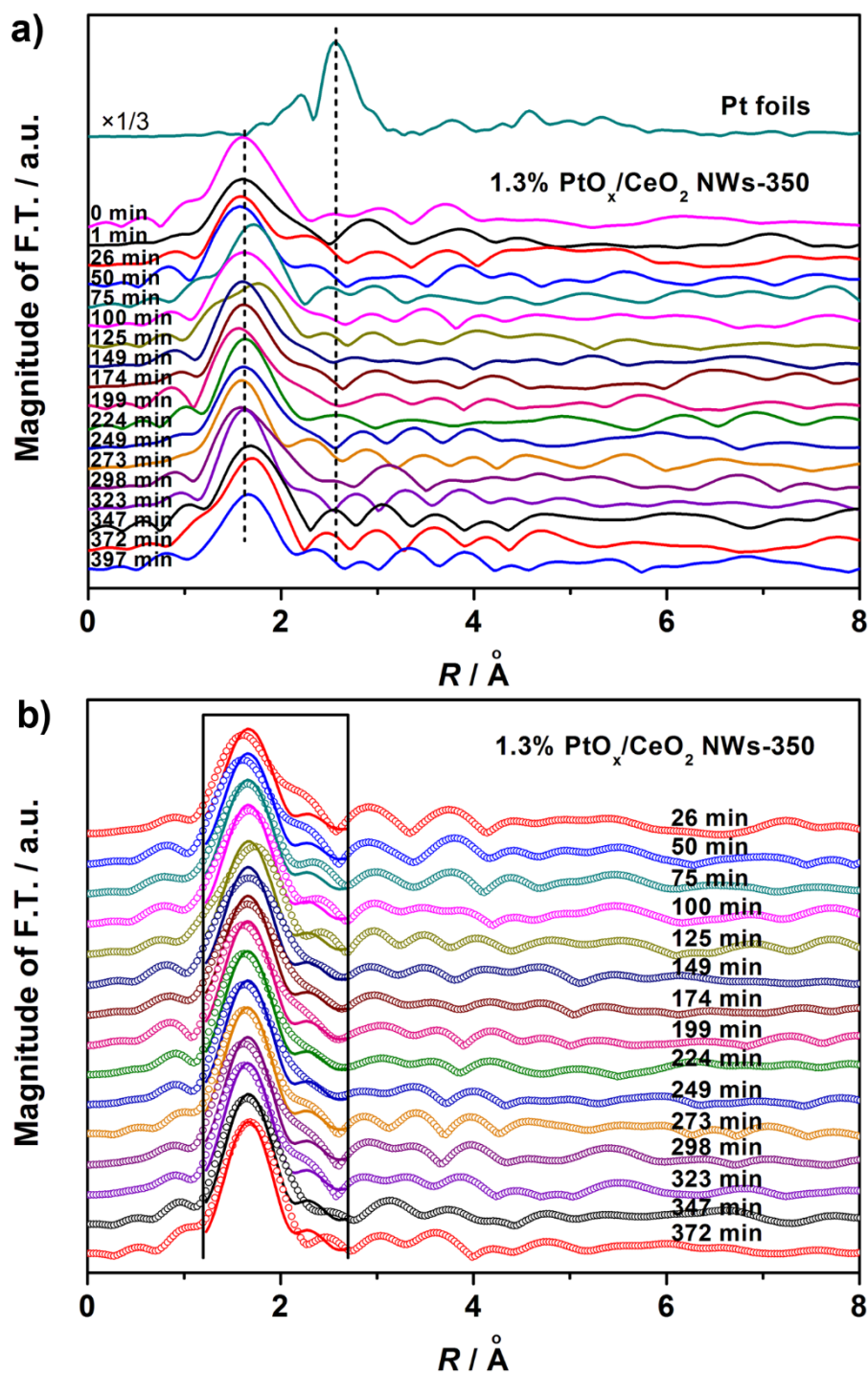
Figure S19. *In-situ* EXAFS analysis of the sample of 1.3% PtO_x/CeO_2 NWs-350 during CO oxidation (2% CO/5% O_2/He, 75 °C). The time labelled on each spectrum represents when the collection of the spectrum started. The collection of each spectrum lasted about 24 min. (a) Fourier transforms of EXAFS spectra of Pt L_3 edge. (b) Fitting curves of the *in-situ* EXAFS spectra. Each spectrum was averaged with the neighbor spectrum before the Fourier transforms and the fitting. The dots represent the experimental data while the solid lines represent the fitted data. The window represents the range in r space involved in the fitting.

Table S9. *In-situ* EXAFS parameters of 1.3% PtO_x/CeO_2 NWs-350 during CO oxidation.[a]

Time / min	Shell	R / Å	N	σ^2 / Å^2	ΔE_0 / eV
26	Pt−O	2.02±0.01	1.7±0.3		
50	Pt−O	2.02±0.01	1.8±0.2		
75	Pt−O	2.02±0.01	1.9±0.3		
100	Pt−O	2.02±0.01	2.0±0.2		
125	Pt−O	2.03±0.01	1.9±0.2		
149	Pt−O	2.02±0.01	2.0±0.2		
174	Pt−O	2.02±0.01	2.0±0.2		
199	Pt−O	2.02±0.01	2.0±0.2	0.002±0.001	14.1±0.5
224	Pt−O	2.02±0.01	2.0±0.2		
249	Pt−O	2.02±0.01	2.1±0.2		
273	Pt−O	2.02±0.01	2.1±0.2		
298	Pt−O	2.02±0.01	2.1±0.3		
323	Pt−O	2.02±0.01	2.2±0.3		
347	Pt−O	2.03±0.01	2.2±0.3		
372	Pt−O	2.03±0.01	2.3±0.3		

[a] N, coordination number; R, interatomic distance between absorber and backscatter atoms; σ^2, Debye–Waller-type factor; ΔE_0, difference between the zero kinetic energy of the sample and that of the model used in the fitting. The time of each data represents when the collection of the spectra started. The collection of each spectrum lasted about 24 min. Athena and Artemis codes were used to extract the data and fit the curve, respectively. Each $\mu(E)$ spectra was averaged with the neighbor spectra before the fitting. Fitting of the Pt−O shell was performed in real space with $\Delta k = 2.7−10$ Å^{-1} and $\Delta R = 1.2−2.7$ Å for Pt (k^2 weighted). The Pt−Pt shell was unable to be clearly fitted. S_0^2 was defined as 0.84 for Pt from the fitting of Pt foil. See Figure S19 for the fitting curves.
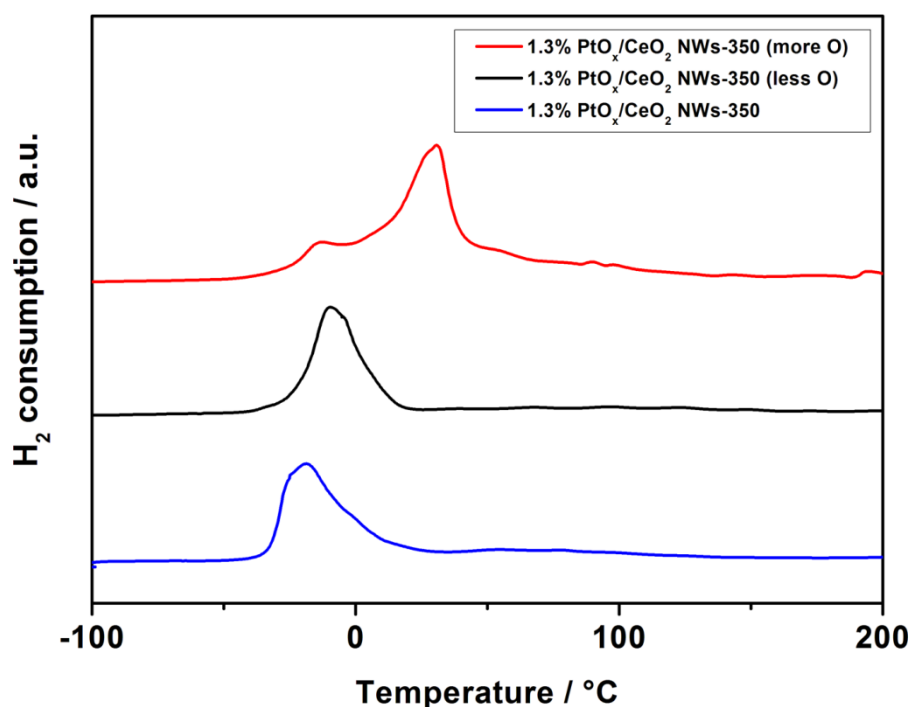
Figure S20. H_2-TPR profiles for the sample of 1.3% PtO_x/CeO_2 NWs-350 after CO treatment (less O) or O_2 treatment (more O) by heating the samples (50 mg) to 200 °C (5 °C/min) in 30 mL/min of flowing 8% H_2/Ar. According to Figure 3, once the PtO_x clusters were reduced, a big amount of oxygen on CeO_2 close to the reduced Pt atoms would be reduced together. The H_2 consumption peak was sensitive to the reducibility of PtO_x. For the sample of PtO_x/CeO_2 NWs-350 (more O), the shift of a big part of the H_2 consumption peak to a higher temperature suggested that the reducibility of a big part of PtO_x on this sample decreased. The increased coordinated oxygen on Pt resulted in the decreased amount of the most active lattice oxygen at $Pt-O_x-Ce$ sites with the highest reducibility.
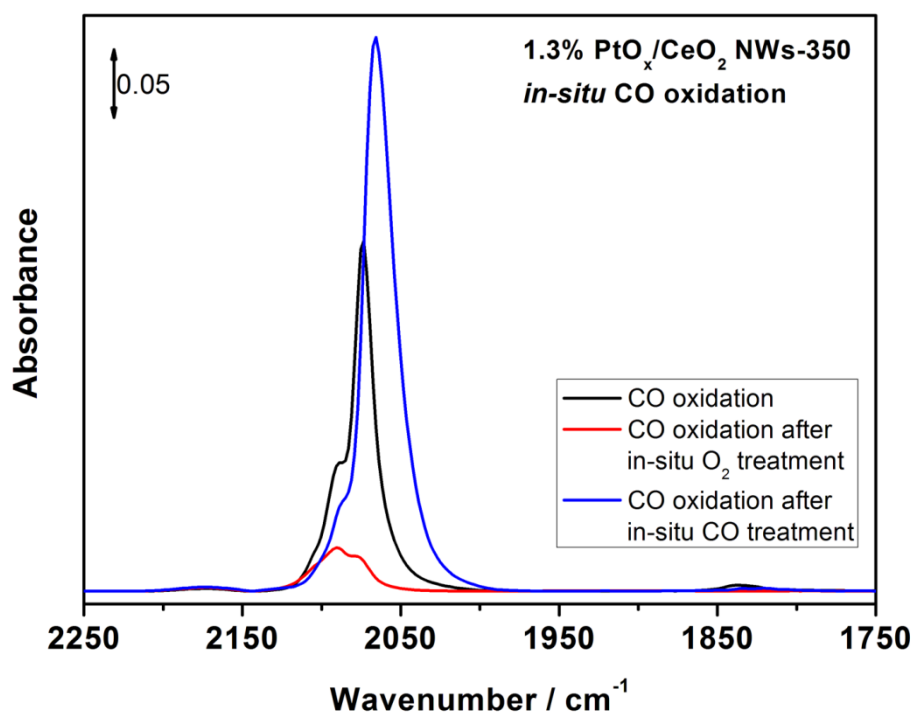
Figure S21. Stabilized *in-situ* IR spectra at 50 °C of CO oxidation over the sample of 1.3% PtO$_x$/CeO$_2$ NWs-350 after CO or O$_2$ treatment. The spectra were collected during the consecutive treatment of the sample in 2% CO/5% O$_2$/He (50 °C 30 min), 5% O$_2$/He (150 °C 30 min), 2% CO/5% O$_2$/He (50 °C 30 min), 5% CO/He (150 °C 30 min), and 2% CO/5% O$_2$/He (50 °C 30 min). According to these *in-situ* IR spectra, CO adsorption was facilitated on the Pt sites with relative low valance on the samples with less coordinated oxygen. On the samples with more coordinated oxygen, CO mainly adsorbed on the oxidized Pt sites, which were found to have deep relation to the inactive sites according to the above discussion. Thus, the oxygen coordinated to Pt sites with high coordination number resulted in the decrease of the density of effective reaction sites.
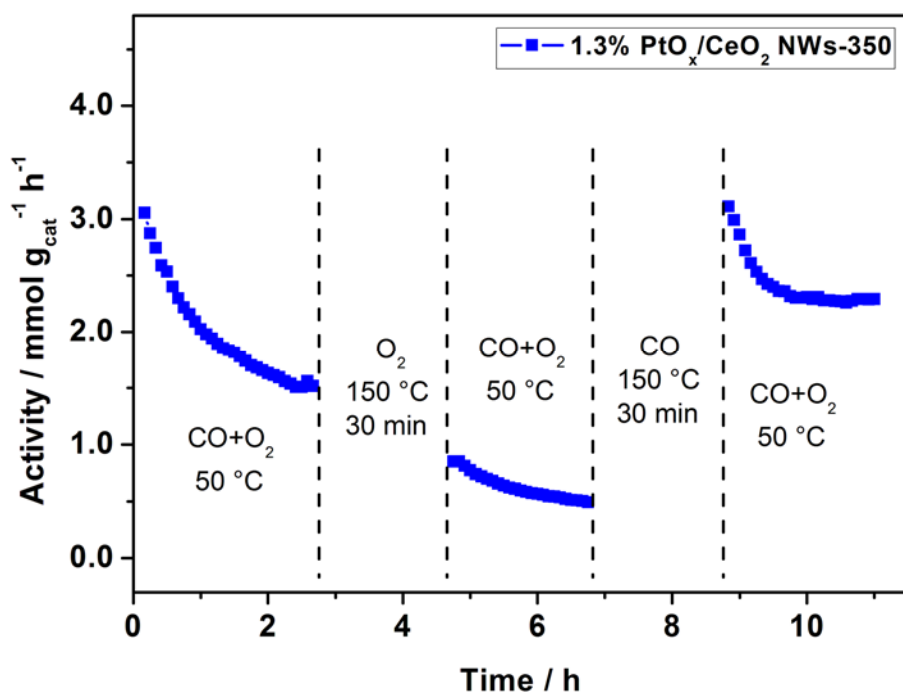
Figure S22. CO oxidation activity of 1.3% PtO$_x$/CeO$_2$ NWs-350 with consecutive redox treatments. The sample was first tested under the CO oxidation condition (13.3% CO/33.3% O$_2$/He at 50 °C), then oxidized in O$_2$ at 150 °C for 30 min, then turned back to the CO oxidation condition, then reduced in CO at 150 °C for 30 min, then turned back to the CO oxidation condition. Oxidation in O$_2$ was similar to the treatment for 1.3% PtO$_x$/CeO$_2$ NWs-350 (more O), and caused the increased CN(Pt−O) according to Table S2, and resulted in the decreased activity. Reduction in CO was similar to the treatment for 1.3% PtO$_x$/CeO$_2$ NWs-350 (less O), and caused the decreased CN(Pt−O) according to Table S2. Some PtO$_x$ sites became active again, leading to the increased activity.
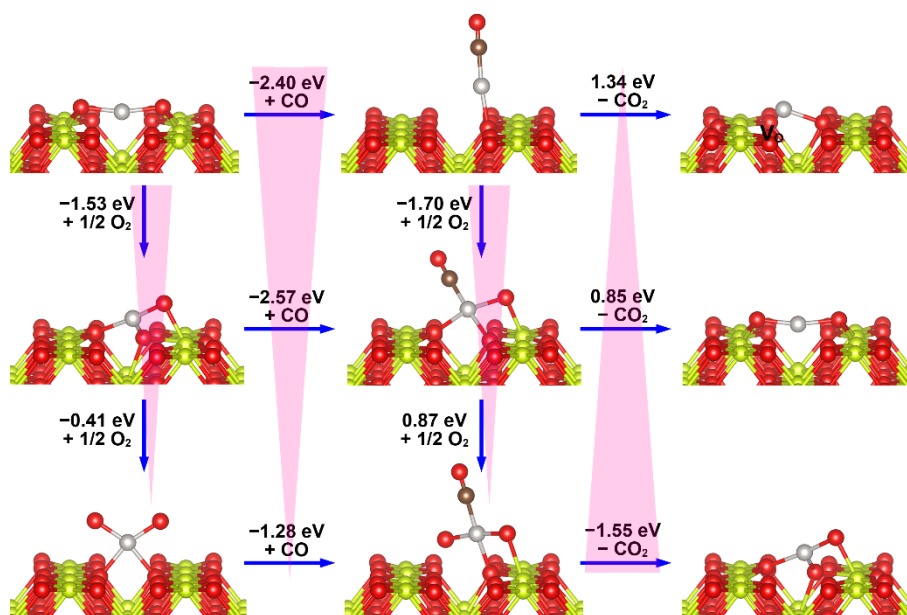
Figure S23. DFT simulation of a single Pt at the O-bridge site on CeO_2 (110) surfaces. CO adsorption, bonding an additional oxygen (oxygen spillover and replenishment), and CO_2 formation on the Pt with varied coordinated oxygen was simulated. The yellow, red, light grey, and dark brown balls represent Ce, O, Pt, and C, respectively. The pink spire-like triangles indicate the approximate variation trends.
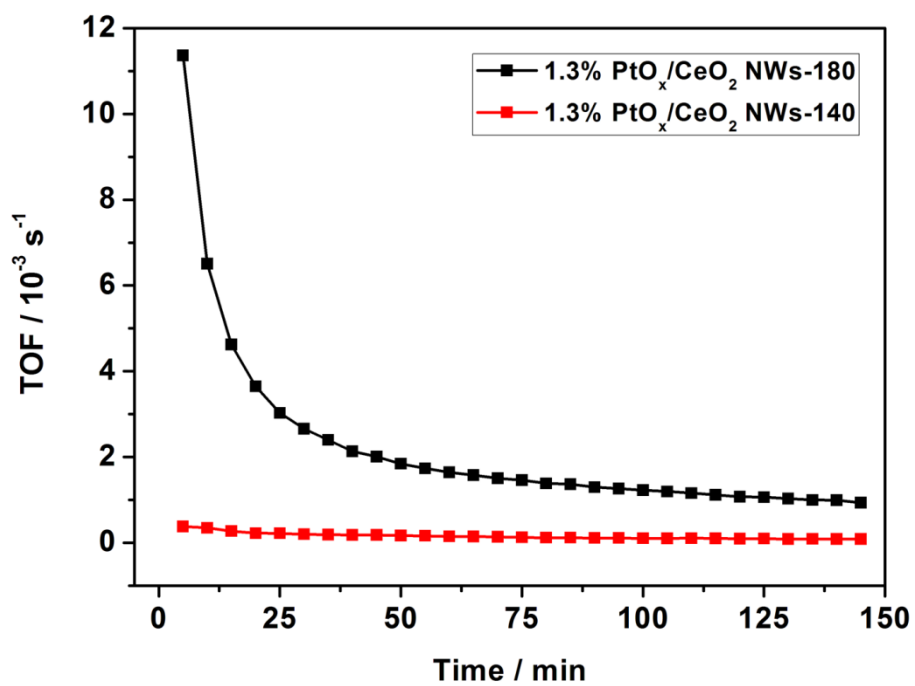
Figure S24. Catalytic activity of 1.3% PtO$_x$/CeO$_2$ NWs-140 after H$_2$ reduction at 180 °C for 10 min (denoted as 1.3% PtO$_x$/CeO$_2$ NWs-180). The sample of 1.3% PtO$_x$/CeO$_2$ NWs-180 was exposed to air before catalytic tests.

References

1. Madier, Y.; Descorme, C.; Le Govic, A. M.; Duprez, D. *J. Phys. Chem. B* **1999**, *103*, 10999−11006.

2. C. Zhang, C.; Grass, M. E.; McDaniel, A. H.; DeCaluwe, S. C.; Gabaly, F. E.; Liu, Z.; McCarty, K. F.; Farrow, R. L.; Linne, M. A.; Hussain, Z.; Jackson, G. S.; Bluhm, H.; Eichhorn, B. W. *Nat. Mater.* **2010**, *9*, 944−949.

3. Salasc, S.; Perrichon, V.; Primet, M.; Chevrier, M.; Mathis, F.; Moral, N. *Catal. Today* **1999**, *50*, 227−235.

4. Liu, H.-H.; Wang, Y.; Jia, A.-P.; Wang, S.-Y.; Luo, M.-F.; Lu, J.-Q. *Appl. Surf. Sci.* **2014**, *314*, 725−734.

5. Wu, Z.; Li, M.; Howe, J.; Meyer, H. M., 3rd; Overbury, S. H. *Langmuir* **2010,** *26*, 16595−16606.

6. Lin, W.; Herzing, A. A.; Kiely, C. J.; Wachs, I. E. *J. Phys. Chem. C* **2008,** *112*, 5942−5951.

7. Daniel, D. W. *J. Phys. Chem.* **1988,** *92*, 3891−3899.

8. Carlsson, P.; Osterlund, L.; Thormahlen, P.; Palmqvist, A.; Fridell, E.; Jansson, J.; Skoglundh, M. *J. Catal.* **2004,** *226*, 422−434.

9. Bera, P.; Gayen, A.; Hegde, M. S.; Lalla, N. P.; Spadaro, L.; Frusteri, F.; Arena, F. *J. Phys. Chem. B* **2003,** *107*, 6122−6130.

10. Jin, T.; Zhou, Y.; Mains, G. J.; White, J. M. *J. Phys. Chem.* **1987,** *91*, 5931−5937.

11. Bazin, P.; Saur, O.; Lavalley, J. C.; Daturi, M.; Blanchard, G. *Phys. Chem. Chem. Phys.* **2005,** *7*, 187−194.

12. Martinez-Arias, A.; Coronado, J. M.; Cataluna, R.; Conesa, J. C.; Soria, J. *J. Phys. Chem. B* **1998,** *102*, 4357−4365.

13. Perrichon, V. *Appl. Catal. A: General* **2004,** *260*, 1−8.